JATIS Journal of Astronomical Telescopes, Instruments, and Systems

RESEARCH PAPER

Emulating and characterizing strong turbulence conditions for space-to-ground optical links: the PICOLO bench

Pablo Robles,[a,b,*] Cyril Petit,[a] Marie-Thérèse Velluet,[a] Louis Le Leuch,[a] Aurélie Montmerle-Bonnefois,[a] Laurie Paillier,[a] Jean-Marc Conan,[a] Frédéric Cassaing,[a,c] Joseph Montri,[a] Benoit Neichel,[b] and Nicolas Védrenne[a]

[a]Paris Saclay University, ONERA, DOTA, Châtillon, France
[b]Aix Marseille University, CNRS, CNES, Laboratoire d'Astrophysique de Marseille, Marseille, France
[c]Paris Saclay University, ONERA, DTIS, Palaiseau, France

ABSTRACT. We present a method to develop a turbulence emulation bench for low-Earth-orbit satellite-to-ground optical communication links under strong turbulence. We provide guidelines to characterize the spatio–temporal dynamics of phase disturbances and scintillation produced by the emulator on a laser beam. We implemented such an emulator for a link at 10 deg elevation and discuss here its design method and characterization. The characterization results are compared to numerical simulations, and this characterization results in the validation of a digital twin of the emulator. The emulator will serve as a testing platform for adaptive optics systems and other free-space optical communication components under strong turbulence conditions.

Keywords: turbulence emulator; strong turbulence; optical telecommunications; adaptive optics; scintillation

Paper 23046G received Apr. 13, 2023; revised Sep. 8, 2023; accepted Nov. 8, 2023; published Dec. 13, 2023.

1 Introduction

Optical communication between satellites and optical ground stations will deliver high speed data transfer between space and Earth.[1,2] In the case of low-Earth orbit (LEO) satellites, higher throughput would enable direct-to-earth (DTE) links, which download high resolution sensor data directly from the satellite hosting the payload to ground. DTE links serve as an alternative to geostationary satellite relay architectures, which may not be available for small constellations.

High data-rate optical communications rely on single-mode fiber coupling for different techniques, such as optical amplification and coherent detection. Unfortunately, the atmospheric turbulence present in the few tens of kilometers close to the ground impacts the quality of the optical beam and hinders fiber coupling,[3] leading to a reduction of the possible data rate due to signal fading.[4] Atmospheric turbulence causes phase distortions on the wavefront of the transmitted laser beam. The use of adaptive optics (AO) provides phase correction of the wavefront and thus improves coupling. However, unlike in traditional astronomical applications, LEO-to-ground links may face strong turbulence conditions that lead to amplitude distortions. The amplitude distortions result in spatio–temporal variations in optical intensity known as scintillation.[5] Scintillation causes variations in the intensity of the received optical signal[6] and impairments in the wavefront measurements.[7] Two factors lead to this strong turbulence regime. First, LEO links

*Address all correspondence to Pablo Robles, pablo.rodriguez_robles@onera.fr

2329-4124/2023/$28.00 © 2023 SPIE

need to work at low elevation angles (desirably down to 10 deg) in order to extend the link duration. At these angles, the propagation distance in the atmosphere is very long (>50 km), leading to a longer propagation path and a larger volume of turbulence crossed, increasing the total turbulence distortion strength. Second, day-time operation faces stronger turbulence due to temperature gradients caused by solar radiation.

In order to test AO systems and optical communication components under strong turbulence, ONERA has developed the PICOLO bench:[8] a turbulence emulation for an LEO-to-ground optical link. This laboratory emulator will complement the current efforts in numerical simulations[9] and experimental tests.[10] The development of satellite-to-ground links requires extensive testing of the different subsystems. Testing with satellites[11–13] is limited by link duration and the lack of LEO satellites equipped with on-board optical terminals. Different ground-to-ground experiments[14–16] have been designed to replicate the conditions of those links, but it is difficult to achieve realistic and reproducible turbulence conditions. Turbulence emulators[17–19] provide well-known, reproducible, and available optical turbulence conditions that enable the testing of AO systems and other optical communication components.

The originality of this work is threefold: first, this emulator is one of the few systems representative of low elevation LEO-to-ground links including phase but also scintillation effects emulation; second, we provide a thorough laboratory characterization of these effects and compare them to numerical simulations; and third, we have produced a digital twin of the laboratory emulator. The digital twin complements the experimental validation of new instrumental concepts in a two-stage process: first, it is used to assess the expected performances and, later, to interpret the experimental results.

This paper reports the method used for the development and characterization of the PICOLO turbulence emulator. In the first part, the main phases of the bench definition will be detailed, in particular the different steps followed to optimize and validate the sampling of the turbulence volume by only three layers and the down-scaling of the experimental setup to be representative of phase and scintillation effects. The second part is devoted to the characterization of the phase and scintillation of the turbulence produced by the bench and a comparison to numerical simulations. Finally, we discuss perspective upgrades of the bench to meet future needs.

2 Optical Turbulence Emulation

Most approaches and experiments for turbulence emulation have been developed for either astronomical cases (i.e., weak turbulence) or horizontal links[20] (i.e., constant turbulence profile), but those do not cover the specific needs of the propagation channel of an LEO-to-ground link at low elevation: multi-layer profile, strong turbulence, and high layer translation speeds. Having multiple layers of turbulence is necessary since satellite-to-ground links are slanted links that go across different atmospheric altitudes. The strong turbulence is a result either of day-light conditions, where turbulence is stronger due to solar radiation, or of low elevations, where the path across the turbulence is longer and therefore turbulence is stronger. Per-layer translation speeds are higher for LEO links since there are two different components: natural wind and apparent wind. Natural wind corresponds to the atmospheric local wind that causes a shifting of the different turbulence layers; its vertical profile depends on the dynamics of the atmosphere. Apparent wind corresponds to the apparent translation of the different turbulence layers due to the relative movement of the line-of-sight with respect to the layers during satellite tracking. The apparent wind speed depends on the angular tracking velocity of the telescope and the distance to a given layer. These speeds are typically an order of magnitude higher at the upper atmospheric layers than the typical wind speeds in astronomical applications; therefore, they represent an additional emulation challenge.

Different methods are available for generating laser beam distortions similar to the ones caused by atmospheric turbulence in a laboratory setup. We discuss briefly the methods available (see Ref. 21 for a more detailed overview) and motivate our choice for the emulator design. We distinguish three methods for turbulence production: passive screens, active screens, and turbulence chambers.

Passive phase screens[22,23] use an optical surface with a fixed phase mask structure providing the optical path difference (OPD) corresponding to atmospheric turbulence distortions. This

mask can be in transmission or reflection. The OPD is generated by controlling the thickness of the surface in a homogeneous optical index medium or by using a controlled inhomogeneous optical index. The phase screens are often mounted on a rotating stage, which produces a shift that approximates the linear displacement of atmospheric turbulence layers due to wind. Since the phase mask pattern used is specified by the user, the phase screens produce deterministic turbulence and can implement profiles by employing one layer per screen. This is a method that has been preferred by several astronomical projects.[24–27] The OPD is engraved on the optical surface by different methods, such as index matching by Lexitek,[23,28] acrylic paint spraying,[24,29] or the cumulative etching by SILIOS Technologies[30] used by several AO systems coordinated by the European Southern Observatory (ESO). This approach ensures an accurate control of the phase distortion but losing versatility, as the distortions are not reconfigurable except by changing the phase screens.

Active phase screens use optical devices, such as spatial light modulators (SLM)[31] and liquid crystal (LC)[32,33] devices, as phase modulators that act as reconfigurable phase screens. Those are able to produce a linear phase displacement (unlike the rotating static phase screens, which only approximate it) and can also combine it with boiling turbulence, as their phase mask is fully programmable. Likewise passive phase screens, active phase screens also create deterministic turbulence and can represent multi-layer profiles. Unfortunately, these solutions pose problems of polarization conservation, chromatism and, more importantly, are limited in reconfiguration rate. Deformable mirrors[34] can provide a higher reconfiguration rate and achromaticity, but present problems related to cost, spatial frequencies, and opto-mechanical design for multi-layer arrangements.

Turbulent fluid chambers create turbulence by mixing two fluids at different temperatures. For example, hot air turbulence chambers[35] use two streams of hot and cold air. The turbulence strength can be modified by changing the temperature difference between the two streams, whereas the wind speed can be regulated by the speed of the fans that inject them into the chamber. Nevertheless, this method is not able to produce the turbulence strength profile characteristic of slanted links, neither is it able to produce the wind speed profile derived from satellite tracking apparent wind. In addition, the turbulence produced cannot be reproduced in a deterministic manner.

A completely different alternative[36] to turbulence emulation uses a variable optical attenuator to create fade profiles in an optical fiber signal derived from numerical simulations (incorporating both turbulence disturbances and the AO system). This is a cost effective solution to emulate a communication channel under the effect of turbulence, with AO correction or not. However, this method requires knowledge of the fiber coupling statistics with AO correction,[37] which are not available for complex AO operating conditions, such as strong turbulence or feeder links precompensation.[38]

Although most turbulence emulators described in the literature target astronomical applications, some were developed for optical communication. For instance, the bench in Ref. 18 is dedicated to the validation of an AO for ground-to-satellite uplink pre-compensation. It is composed of a single phase screen and presents an underestimated beam wandering due to a scaling problem. The emulator in Ref. 19 is representative of an uplink at 30 deg elevation, so it does not focus on a strong turbulence case and the effect of scintillation. Finally, the work in Ref. 17 uses two SLMs with an intermediate reflection to produce a second footprint on each SLM, obtaining four different phase screens. The emulated link corresponds to strong atmospheric turbulence, but the link is horizontal and there is no detailed characterization of the scintillation produced on the beam. In summary, the existing emulators target different cases, and therefore answer trade-offs different from ours, but a detailed methodology for the characterization of phase and amplitude fluctuations is usually lacking.

For our emulator, we decided to use passive phase screens mounted on rotation stages, with the possibility of using an SLM to introduce additional boiling turbulence or bursts of turbulence. Several criteria were considered in this decision: (1) to specify a precise turbulence strength with the correct statistics, (2) to reproduce the delivered turbulence conditions, (3) to produce strong enough turbulence (high phase modulation dynamic), and (4) to be able to adjust the speed of every layer to the strong apparent displacements due to satellite tracking.

3 Bench Definition

The definition of the bench started with the selection of a reference turbulence profile. We compressed the profile to a three-layer profile that could be implemented on the bench as phase screens (see Sec. 3.1). The profile was then geometrically scaled to reduce its size so it can fit on an optical table (see Sec. 3.2). We specified and procured the manufacturing of the three phase screens according to the selected three-layer profile (see Sec. 3.3). Finally, we designed the optomechanics that allow propagating a laser beam through the turbulence emulator and providing the generated turbulence to a client system and an analysis camera (see Sec. 3.4).

3.1 Turbulence Profile Compression

We used as reference profile a modified Hufnagel-Valley 5/7 model[39] (following the *ITU-R P.*1621-2 recommendation) with a turbulence strength at the ground surface level of $C_n^2 = 1 \times 10^{-13}$ m$^{-2/3}$ and an upper-level wind speed of $V_{\text{rms}} = 21$ m/s that influences the turbulence strength of the upper layers of the atmosphere. Another possibility for the profile selection is to use a database of *in situ* C_n^2 profile measurements to define typical or worst-case profiles.[40,41] Note that our overall emulator design methodology does not depend on the selection of the reference profile.

The reference profile was first compressed to a 50-layer profile to allow Monte–Carlo numerical simulations. The compression to 50 layers is carried by optimization of layer height and strength under the condition of keeping constant the following turbulence integrated parameters: r_0 as a quantification of the phase distortion strength, θ_0 for the anisoplanatism, and σ_χ^2 for the scintillation strength. The method is similar to the methods presented in Ref. 42 but including the scintillation effects too.

A second profile compression was necessary to reduce the number of phase screens required for the implementation of the emulator. The number of layers, and therefore phase screens, on the emulator, should be limited in order to reduce the system's complexity and cost. At the same time, a multi-layer profile is also needed to generate a representative turbulence profile: with the proper representation of phase and scintillation effects and the corresponding temporal dynamics derived from the natural and apparent wind profiles. In addition, the use of several screens limits the periodicity in the generated turbulence (see Sec. 4.2.5 for a discussion on the periodicity).

We decided to use three layers since we consider that three layers allow representing qualitatively the scintillation characteristics of the link. In fact, the scintillation irradiation pattern depends on both turbulence strength and propagation distance, therefore we can design each of the three layers to represent one of the possible combinations and its resulting scintillation. The first layer is located at the telescope pupil and emulates the atmospheric ground layer: very strong in turbulence but with short propagation distance, so negligible scintillation contribution. The time evolution of this layer is mainly driven by natural wind, i.e., slow layer speed (typical order of magnitude 10 m/s). The second layer is located at a more significant propagation distance. This will produce a typical size of the irradiation pattern smaller than the size of the telescope pupil. When using a Shack–Hartmann wavefront sensor, the typical size of the irradiation pattern is similar to the size of one of the subpupils, so scintillation contributes to the flux variation at the subpupil level, impairing wavefront sensing. The third layer will be located far away and will represent the free atmosphere: weaker turbulence but with a long propagation path. The resulting typical size of the irradiation pattern will have a size close to the telescope pupil, which contributes to the variation of available flux with time, and therefore the stability of the signal regardless of the AO performance. The temporal evolution of the second and third layers is mostly driven by the apparent wind component due to LEO satellite tracking, i.e., very fast layer speed (typical order of magnitude 150 m/s).

While 50 layers are enough to properly represent the original turbulence profile, the restriction to three layers poses a greater challenge. The first layer was fixed to be at the telescope pupil. The positions and strengths of the second and third layers were found using the same optimization based on integrated parameters as for the 50-layer profile. The natural wind velocity profile was chosen as 10, 15, and 30 m/s, respectively, whereas the apparent wind is computed from the satellite tracking slew rate and the distance to the corresponding layer. We consider a 10 deg elevation and an orbit altitude of 500 km that result in a slew rate of 3.834 mrad $\cdot$ s^{-1}.

Table 1 Integrated turbulence parameters for the 50-layer profile and the compressed three-layer profile.

Parameter	50-layer	Three-layer
r_0 (cm)	2.56	2.56
θ_0 (μrad)	1.75	1.68
τ_0 (μs)	338	315
σ_χ^2	0.58	0.58

Table 1 reports the integrated parameters of the 50-layer and the three-layer profiles. It can be observed that the compression of the profile managed to keep the targeted integrated parameters very close. A more detailed comparison of the 50-layer and the three-layer profiles is available in Ref. 8.

3.2 Propagation Path Geometrical Scaling

We performed a down-scaling of the link geometry in order to fit it within a laboratory optical table. The complete process is a trade-off between available technologies for phase screen manufacturing (including resolution and stroke), opto-mechanical design, and required space (as we wish to keep the system compact). We provide a simplified discussion of this trade-off.

To achieve a physically equivalent system in terms of turbulence and diffractive effects, the down-scaling must preserve the following dimensionless groups constant: $D/\sqrt{\lambda L}$ for layer at distance L and a telescope of diameter D to be representative of scintillation effects on the pupil due to each layer; D/r_0 and the contribution to it of each layer through the $C_n^2 \cdot dz$ profile; and finally $V/(D \cdot f_{\text{samp}})$, which relates the layer displacement in a sampling interval to the size of the pupil. In the following, for each parameter X we use the notation X_{sky} for its value on sky and X_{bench} for its effective value on the bench and express the relationships between them.

Conservation of scintillation effects leads to

$$D_{\text{bench}} = \sqrt{\frac{L_{\text{sky}}}{L_{\text{bench}}}} \cdot D_{\text{sky}}, \tag{1}$$

$D_{\text{bench}}/D_{\text{sky}} = \sqrt{L_{\text{sky}}/L_{\text{bench}}}$ is a geometric compression factor defined by the ratio between the initial and final propagation lengths. The maximum propagation distance available from the top layer to the telescope will therefore drive the scaling of the telescope diameter. At the same time, reducing the total propagation distance requires reducing the telescope diameter too. The telescope diameter in the bench defines the beam footprint on the phase screens; therefore, it cannot be reduced too much, otherwise, the resolution of the manufacturing of the screens limits the turbulence that can be achieved.

Considering conservation of D/r_0, the turbulence strength is down-scaled as

$$r_{0,\text{bench}} = \frac{D_{\text{bench}}}{D_{\text{sky}}} \cdot r_{0,\text{sky}}. \tag{2}$$

To obtain the downscaling of the $C_n^2 \cdot dz$ of every layer, we use $r_{0,\text{bench}}$. Since the relative $C_n^2 \cdot dz$ profile is conserved, the absolute values of $C_n^2 \cdot dz$ can be scaled to achieve $r_{0,\text{bench}}$.

Finally, each layer's velocity depends on two factors: the relationship between diameters and a temporal scaling factor. For a given layer the velocity is down-scaled as

$$V_{\text{bench}} = \frac{D_{\text{bench}}}{D_{\text{sky}}} \cdot \frac{f_{\text{samp,bench}}}{f_{\text{samp,sky}}} \cdot V_{\text{sky}} = \frac{D_{\text{bench}}}{D_{\text{sky}}} \cdot \frac{1}{\tau} \cdot V_{\text{sky}}. \tag{3}$$

The first factor of the last right hand term is related to the previously defined geometric compression factor. The second factor, $\tau = f_{\text{samp,sky}}/f_{\text{samp,bench}}$, is a time scaling factor and it allows a temporal down-scaling of the layer speeds, by operating the bench at lower sampling

Table 2 Resulting geometric down-scaling for the different phase screens.

Parameter	On-sky	Bench
Propagation distance	57 km	1.4 m
Pupil diameter	0.4 m	2 mm
Wavelength, λ, (μm)	1.55	1.55
Layer 1		
Position, z	0 m (pupil)	0 m (pupil)
Wind speed, V, (m/s)	10.00	5×10^{-4}
Layer 2		
Position, z	2.88 km	0.072 m
Wind speed, V, (m/s)	26.04	1.3×10^{-3}
Layer 3		
Position, z	57.8 km	1.4 m
Wind speed, V, (m/s)	250.84	1.2×10^{-2}

frequency. As a result, any time interval Δt_{sky} on the original system is equivalent to $\Delta t_{\text{bench}} = \tau \cdot \Delta t_{\text{sky}}$ on the down-scaled system.

For example, for an AO system working at a 5 kHz sampling frequency on-sky and 50 Hz on the bench, the equivalent time scaling factor is $\tau = 5000/50 = 100$, this means that everything on the emulator runs 100 times slower than on-sky. For the same reason, to acquire a time series of $\Delta t_{\text{sky}} = 60$ s of duration, it would be necessary to record during $\Delta t_{\text{bench}} = \tau \cdot \Delta t_{\text{sky}} = 100 \cdot 60 \text{ s} = 100$ min on the bench.

Ideally, one would test a system with $\tau = 1$, so the system operates at its nominal frequency. Two different factors make temporal scaling convenient: first, reducing the rotational speed of the phase screens and second, allowing the use of slower components in the emulator or client system. Indeed, due to the apparent wind speed of the LEO satellite, the upper layer speed is quite high, so high that the rotational speed of the phase screen to achieve such a layer velocity would push the limits of the rotation stage and produce possible vibrations and safety issues in case of component malfunction. In addition, the PICOLO bench is dedicated to the development and testing of new concepts and systems, cases in which it may not be possible to run certain components as fast as in operational conditions on sky. Temporal scaling is then a useful option. As an example, operating at slower time scale also allows the use of an SLM, located in the pupil, which operation is usually limited at 50 Hz, to add user-defined non stationary turbulence, bursts, or specific perturbations. Finally, during the characterization of the bench, the infrared camera used is limited to an acquisition frequency of 100 Hz, so the scaling was also necessary during the characterization to obtain an equivalent sampling frequency of 10 kHz.

Note that the geometrical scaling of the emulator is independent of the diameter chosen for the telescope since the relationships are all in terms of the ratio $D_{\text{bench}}/D_{\text{sky}} = \sqrt{L_{\text{sky}}/L_{\text{bench}}}$. If one would like to change the telescope diameter, one could compute D_{bench} using Eq. (1) and the optical propagation characteristics in the emulator would not change.

In the following, we provide the scaling for our implementation of the emulator. We wish to have a telescope diameter in the bench equivalent to $D_{\text{sky}} = 40$ cm diameter telescope on-sky. The results of the scaling exercise are summarized in Table 2. From the top layer, the propagation distance toward the telescope is $L_{\text{sky}} = 57$ km on sky, and we want to limit the maximum propagation distance on the bench to 1.4 m. Equation (1) leads to a telescope pupil of $D_{\text{bench}} = 2$ mm. The wavelength is the same on the bench: $\lambda_{\text{sky}} = \lambda_{\text{bench}} = 1.55$ μm. For the temporal down-scaling, we consider two scenarios: one where an $f_{\text{samp,sky}} = 5$ kHz is equivalent to $f_{\text{samp,bench}} = 2$ kHz, close to the current AO systems, and one where $f_{\text{samp,sky}} = 5$ kHz is

Table 3 Summary of the different three-layer profiles considered in this work.

		$C_n^2 \cdot dz$ ($m^{\frac{1}{3}}$)		
Layer	z	Compressed	Specified	Measured
Layer 1	0 m (pupil)	4.615×10^{-11}	2.545×10^{-11}	2.563×10^{-11}
Layer 2	2.88 km	1.605×10^{-11}	1.616×10^{-11}	1.396×10^{-11}
Layer 3	57.8 km	8.492×10^{-13}	8.553×10^{-13}	1.015×10^{-12}

equivalent to $f_{\text{samp,bench}} = 50$ Hz for testing new components that cannot work at higher rates at the moment. The layer velocities in the table are reported for the later case, $f_{\text{samp,bench}} = 50$ Hz, and they must be multiplied by 40 for an AO loop running at $f_{\text{samp,bench}} = 2$ kHz. These values lead to acceptable specifications for the procurement of the phase screens and their rotating stages while achieving a compact bench design.

3.3 Phase Screen Specification

The phase screens have been manufactured by the company SILIOS Technologies. We have provided the phase screen specification as a two-dimensional (2D) phase map of the desired phase. The maps were generated from the specified r_0 and L_0 for each layer and with a von Kármán spectrum. The maps where scaled to keep the same relationship with respect to the telescope diameter after the down-scaling of the bench. The phase screens are manufactured with a 40 μm resolution, which for a $D_{\text{bench}} = 2$ mm and $D_{\text{sky}} = 0.4$ m is equivalent to a maximum spatial frequency representation of 62.5 cycle $\cdot$ m^{-1} on-sky.

The technical constraints in the manufacturing process lead to reducing the turbulence strength in PS1, the strongest layer, since the resulting peak-to-valley distance in the screen was not attainable. This resulted in a change of the specification of $C_n^2 \cdot dz$ from 4.615×10^{-11} $m^{\frac{1}{3}}$ to 2.545×10^{-11} $m^{\frac{1}{3}}$. The change in the turbulence strength of PS1 results in a change of the global r_0 from 2.6 to 3.3 cm, whereas the scintillation characteristics remain the same since PS1 is located at the pupil of the telescope. This loss of turbulence strength was considered acceptable since it does not affect the scintillation characteristics.

Table 3 summarizes the different profiles used in this work. All $C_n^2 \cdot dz$ values provided correspond to the on-sky values, i.e., before down-scaling. All the numerical simulations conducted in this work simulate the equivalent on-sky system and therefore use these values. The "compressed" profile corresponds to the compression from the original 50-layer profile to a three-layer profile (see Sec. 3.1). The "specified" profile corresponds to the profile specified to the phase screen manufacturer, where the strength of layer 1 had to be reduced due to manufacturing constraints (see Sec. 3.3). Finally, the "measured" profile corresponds to the profile measured during the phase characterization of the screens (see Sec. 4.1). This is the profile used in Sec. 4.2 for the numerical simulations that are compared to the characterization measurements, it is therefore considered as the most representative with respect to the experimental setup.

3.4 Opto-Mechanical Design

Figure 1 shows the opto-mechanical layout of the bench, and Fig. 2 provides an image of the bench implementation. The main optical path is marked with a red line. A laser source is injected in the bench using a fiber collimator. A first phase screen (PS3) is positioned close to the source at the highest altitude, whereas PS2 is close to the ground and PS1 is located as close as possible to the entrance pupil of the telescope. The screens are placed on rotation stages. Two mirrors mounted on tip-tilt stages allow proper alignment of the input beam. A filter wheel equipped with neutral density filters allows different power attenuation levels on the laser input.

The telescope is emulated by a combination of lenses. The entrance pupil of the telescope is located at a mechanical stop in front of the first lens of the telescope. We use afocal lens systems to re-image the pupil plane and re-scale it. The output beam of the telescope is finally collimated.

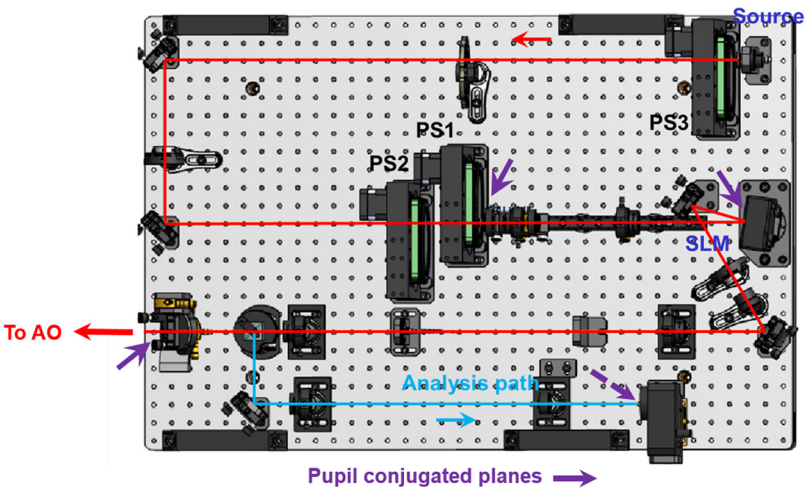

Fig. 1 Opto-mechanical design of the PICOLO turbulence emulator.

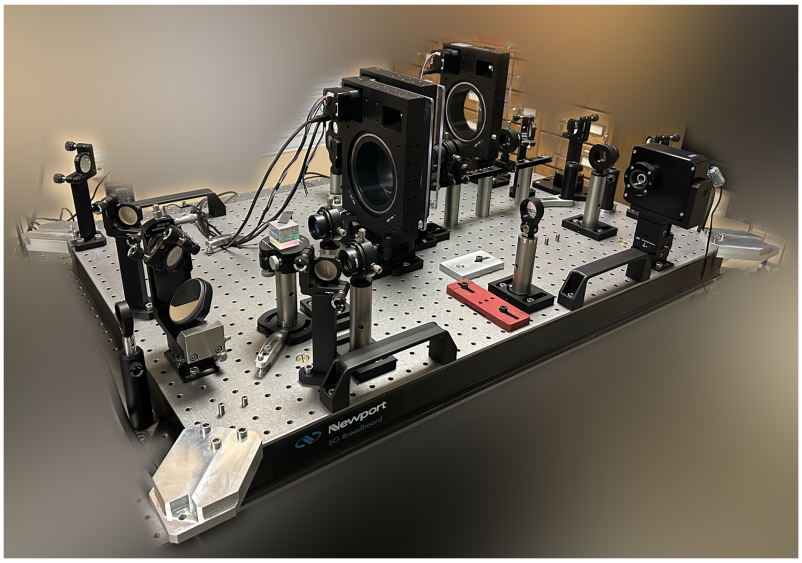

Fig. 2 Image of the implementation of the PICOLO bench.

A periscope is placed at the output of this main path to ease coupling with a client system. The second path (in blue) is dedicated to the analysis of the perturbated beam. A beamsplitter picks a fraction of the flux and sends it to a near-infrared camera. A flip lens allows to switch between focal plane and pupil plane imaging on the camera. Three planes are conjugated to the entrance pupil (marked with a purple arrow): the first may accept an SLM, though it is a plane mirror for the moment; the second to the first mirror of the output periscope; and the third to the infrared camera (if in pupil imaging configuration). The emulator is integrated on a 600 mm $\times$ 900 mm optical breadboard.

4 Characterization

We present here our methodology for the characterization of the turbulent link channel emulator. The goal of this characterization is to ensure that the phase screens have been properly manufactured, that the emulator produces the correct turbulence conditions, and that those are understood.

We provide measurements of both phase and scintillation on both a per-screen basis and for the three-screen configuration. The study of scintillation covers both its spatial and temporal

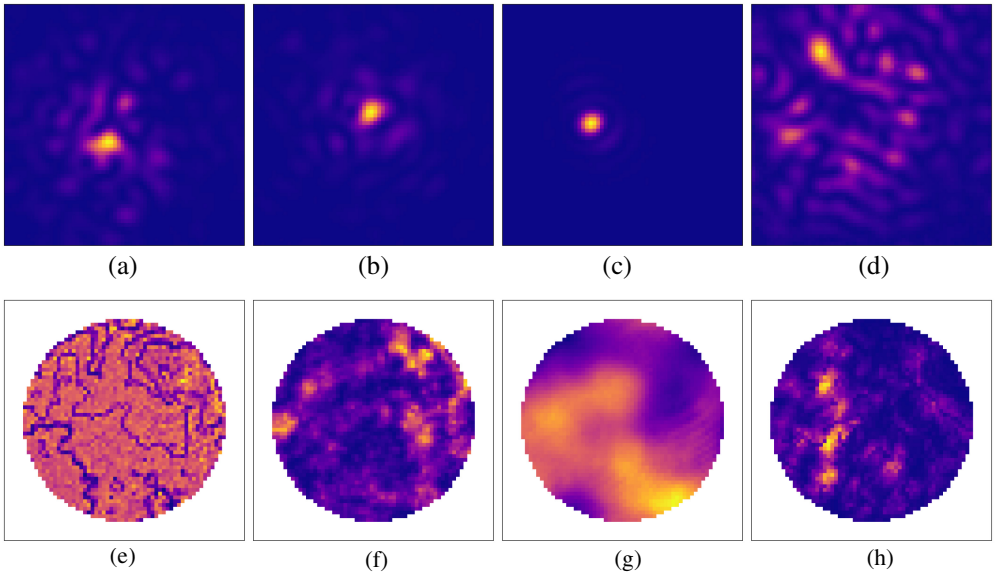

Fig. 3 Exemplary experimental acquisitions of short-exposure PSF and pupil images for the different phase screen configurations. (a) PSF, PS1 at P1, (b) PSF, PS2 at P2, (c) PSF, PS3 at P3, (d) PSF, all, (e) pupil, PS1 at P1, (f) pupil, PS2 at P2, (g) pupil, PS3 at P3, and (h) pupil, all.

behavior. We also compare the results to a numerical simulation of the emulator using TURANDOT,[9] an optical physics propagation tool developed by ONERA for CNES (the French Space Agency). The result of this comparison is a digital twin of the PICOLO bench to support cross-validation between experiments and simulations during future developments.

4.1 Phase Characterization

Different methods are possible to characterize the phase introduced by the phase screens and verify that they provide the desired phase distortions in terms of phase variance and spectrum. A first method[43] uses the measurement of the full-width-half-maximum of the long-exposure seeing-limited point spread function (PSF) and compares it to the theoretical expectation from the prescribed phase. This method is not applicable on the bench in our case due to both the strong beam wander (resulting in PSF cropping) and speckles in the PSF derived from the strong turbulence conditions (see Fig. 3). Alternatively, we chose to use a dedicated set-up to measure wavefront slopes with a Shack–Hartmann wavefront sensor, reconstruct the phase associated with these measurements, and compare the reconstructed phase statistics to the statistics of the prescribed phase screens. The phase reconstruction is conducted using a Zernike polynomials basis, obtaining modal variances for each mode. To compare the estimated modal phase variances to the screen prescription, a theoretical model of these variances assuming a von Kármán spectrum is fitted using the two model parameters: the Fried number (r_0) and outer scale (L_0). The fitting provides an estimation of these two parameters, which can be compared to corresponding values for each of the prescribed phase screens. The details of this method and the required setup are discussed in the next section.

The phase characterization presented here was the method used to accept the phase screens from the manufacturer while further characterization was conducted after acceptance. The characterization of the scintillation power spectral densities in Sec. 4.2 provides supplementary phase verification since the scintillation characteristics depend on the phase.

4.1.1 *Measurement setup*

We first obtained Shack–Hartmann measurements of the phase screens, to achieve that we illuminated a circular section of the phase screen with a collimated laser source at a wavelength $\lambda = 1.55$ μm. A $4f$ imaging relay was used to conjugate the footprint of the collimated beam on the phase screen to the pupil of the Shack–Hartmann wavefront sensor. Conjugation of

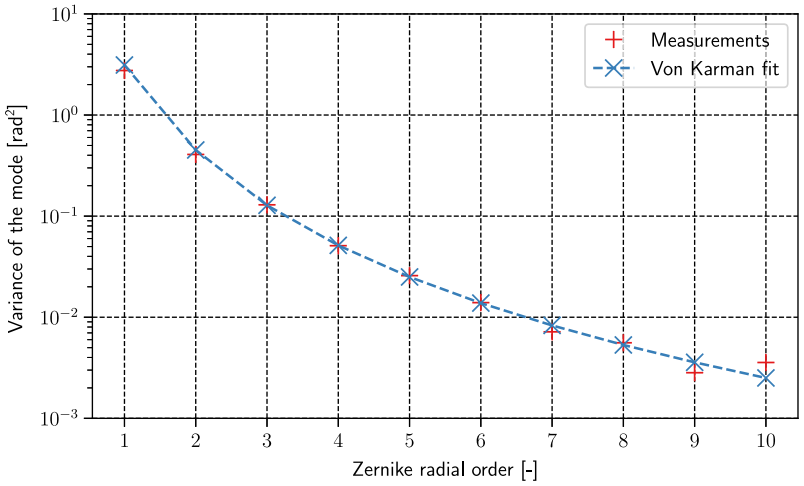

Fig. 4 Reconstructed Zernike mode variances versus their fit to a von Kármán spectrum for PS2.

the planes avoids further propagation of the wave between the phase screen and the wavefront sensor, which would produce scintillation and therefore bias the wavefront measurement. The Shack–Hartmann wavefront sensor used is an *Imagine Optic HASO4 SWIR 1550*, which is capable of providing absolute slope measurements due to the calibration provided by its manufacturer.

The collimator beam footprint was placed at the same distance from the center of rotation of the phase screen as used in the bench. Different samples of the screen were taken by rotating the screen. We decided to measure only the disk that will be illuminated during the rotation of the phase screens since the distance between the rotation center and the beam footprint is constant. This strategy ignores the rest of the screen and provides a limited number of measurements; however, it corresponds to a characterization of the only area of the phase screen that is used. The total number of statistically independent measurements available is around 50 per phase screen; although overlapping measurements were used to average measurement noise even if they do not bring statistical convergence. The same discussion applies to the scintillation characterization.

The acquired slope measurements were used to reconstruct the Zernike coefficients (using the least-squares method[44]) for each spatial sample; the variance of each coefficient across all samples provides an estimation of the variance for the corresponding Zernike mode. We chose to reconstruct up to the 10$^{\text{th}}$ Zernike polynomials radial order, considering the number of available Shack–Hartmann subpupils. The resulting Zernike modes variances were averaged by radial order and fitted to their theoretical values assuming a von Kármán spectrum[45] using as fitting parameters the Fried number (r_0) and outer scale (L_0). The fitting was computed by solving a non-linear least squares problem using a Levenberg–Marquardt optimization routine. Special attention needs to be paid to the fitting: The modal variance of the atmospheric turbulence follows a power law with very different orders of magnitudes between radial orders (see Fig. 4); if the least squares cost function is computed using all modal variances, the low order modes, which have bigger variances, will dominate the fitting and bias the estimation. In the von Kármán spectrum, the low radial order modes are influenced by both the outer scale and the Fried parameter, whereas the high radial order modes are only influenced by r_0. As a result, r_0 can be estimated by first fitting the high radial orders to a von Kármán spectrum with a fixed outer scale; we use the Kolmogorov spectrum, which is equivalent to an infinite outer scale. A second fitting of all modal variances is used to estimate L_0, this time assuming a von Kármán spectrum with the previously estimated r_0 as a fixed parameter.

4.1.2 *Results*

Figure 4 shows, for the case of PS2, the measured Zernike coefficient variances averaged per radial order and a comparison to the best fit to a von Kármán spectrum. The close fitting of the

Table 4 Reconstructed Zernike mode variances fitting results to von Kármán spectrum.

Screen	D/r_0 theo.	D/r_0 meas.	L_0/D theo.	L_0/D meas.
PS1	8.889	8.964	3.000	3.945
PS2	6.780	6.227	3.000	8.585
PS3	1.159	1.292	10.000	16.592

measurements to the theoretical spectrum shape confirms that the measured phase follows the power law of the von Kármán spectrum. The deviations at higher radial orders (i.e., high spatial frequencies) are related to noise propagation and the reconstruction of higher Zernike orders (aliasing effect). The results of the Zernike mode variance fitting for the three screens are summarized in Table 4 by means of the resulting r_0 and L_0 estimates. In terms of relative error between the expected and the measured quantities, r_0 error is 10% in the worst case, whereas for L_0 it can be as high as 65%. The bigger mismatch in L_0 can be explained by the difficulty of estimating the variance at low spatial frequencies with a limited number of measurements; since low frequencies have fewer periods over one measurement, it is necessary to use more measurements to estimate low spatial frequencies than to estimate high frequencies. This lack of accuracy could be improved in the future by increasing the number of available phase measurements by measuring all the phase screen area and not only the annular section that is illuminated during the operation of the bench.

In conclusion, these results provide an estimation of the r_0 and L_0 of the screens and confirm that they follow the desired von Kármán spectrum in their spatial statistics. This first characterization allowed us to test the quality of the phase screens and accept them. The later characterization of the scintillation presented in the next section served as a supplementary characterization of the phase produced by the screens. We also used the measured per-screen r_0 to derive the equivalent $C_n^2 \cdot dz$ for each screen, reported in Table 3 as "measured" profile. These values were used for the numerical simulations of the wave propagation in the bench.

4.2 Scintillation Characterization

Optical wave scintillation, unlike phase, can be directly measured as intensity on the pupil plane. We characterized the scintillation on the emulator by analyzing images of irradiance patterns on the pupil using a matrix detector. The scintillation characterization was conducted in both spatial and temporal domains. We compared the measured results to a numerical simulation of the same propagation case. This results in a cross-validation of the specification of the phase screens and the resulting spatial and temporal signatures for scintillation.

4.2.1 *Measurement Setup*

As pointed out in Sec. 3.4, the bench allows pupil imaging by an afocal telescope that relays the pupil plane from the telescope entrance aperture to an imaging matrix detector. This allows recording the irradiance distribution (i.e., sampled value proportional to the irradiance on each pixel in $\mathrm{W} \cdot \mathrm{m}^{-2}$) over the pupil of the system, which is used to characterize the scintillation.

The acquisitions are taken in two different ways for spatial and temporal characterization. For spatial characterization, the phase screens are rotated so that for every acquisition the beam footprints on the screen do not overlap. In this way, we reduce the spatial correlation between measurements. For temporal characterization, the phase screens are rotated to a speed that produces the equivalent layer velocity for the given layer, achieving the desired temporal correlation.

For the spatial characterization, the integration time and the screen rotational speed were adjusted to reduce the displacement during exposure to less than a 10th of the pixel size, therefore negligible. In the case of the temporal characterization, the 50 μs exposure time used is equivalent to a 500 ns exposure time on-sky (see the temporal compression discussed in Sec. 3.2) and as a result negligible too.

The bottom row of Fig. 3 presents a typical image of the experimental acquisitions of pupil irradiance patterns used for scintillation characterization.

We carried all characterizations first on a per-screen basis and later with the three screens together. The individual screen characterization provides the verification of every screen, whereas the three-screen setup characterizes the operating conditions of the bench.

The fiber collimator used as source (i.e., emitter) beam has a 7 mm beam waist diameter at the pupil of the telescope, whereas the pupil is 2 mm. This results in a truncated Gaussian illumination pattern on the pupil. The effect of the Gaussian shape and its wandering was confirmed to be negligible via numerical simulations. As a result, the rest of the numerical simulations conducted do not model this effect and consider a homogeneous illumination pattern.

4.2.2 *Numerical simulations*

We compared the experimental results to numerical simulations using the optical propagation code TURANDOT. The numerical simulation does not use the phase maps specified to the manufacturer. Instead, it generates phase screens with von Kármán statistics and a $C_n^2 \cdot dz$ reported as "measured" profile in Table 3, which was derived from the fitting of r_0 summarized in Table 4. As a consequence, the results of the numerical simulations are expected to be statistically equivalent to the perturbations generated by the emulator but not strictly the same. For spatial characterization statistics, each realization uses news statistically independent draws of the phase screens from the prescribed $C_n^2 \cdot dz$. For the temporal characteristics, a time series is generated from a unique realization of the phase screens, for each time step the layers are shifted according to their wind speed achieving the time series. After propagation, the irradiance over the pupil is computed, obtaining the equivalent of the experimental measurements. Once the equivalent data to the experiment are produced, experiment and simulation data are post-processed in the same fashion.

The numerical simulations do not contain any measurement noise in the resulting irradiance. This is not the case for the experimental measurements, where read-out noise and shot noise are not negligible. The laser power was adjusted to be as high as possible during the characterization. This is limited by the saturation of the matrix detector pixels due to the finite dynamic range, whereas the dynamic range (i.e., variance) of the scintillation speckles increases with the turbulence strength.

4.2.3 *Characterization metrics*

We characterize scintillation by two main metrics: the power spectral density of the normalized irradiance distribution over the pupil and the scintillation index.

First, we define a normalization of $\mathcal{I}(x, y, k)$, the irradiance distribution across the spatial coordinates x and y, with k being either a temporal or an ensemble index:

$$\overline{\mathcal{I}}(x, y, k) = \frac{\mathcal{I}(x, y, k) - \langle \mathcal{I} \rangle_k (x, y)}{\langle \mathcal{I} \rangle_k (x, y)}, \tag{4}$$

where the bracket operation corresponds to the sample average of the magnitude, defined in general as $\langle \mathcal{I}(x, y, k) \rangle_{x,y,k} = \Sigma_{i_x=1}^{N_x} \Sigma_{i_y=1}^{N_y} \Sigma_{i_k=1}^{N_k} X(x_{i_x}, y_{i_y}, k_{i_k}) / (N_x \cdot N_y \cdot N_k)$, whereas in this case it is $\langle \mathcal{I}(x, y, k) \rangle_k = \Sigma_{i_k=1}^{N_k} X(x, y, k_{i_k}) / N_k$. Note that the normalization is different for each pixel over the pupil of the telescope, therefore it allows the comparison of the scintillation regardless of the average irradiance impinging on the pupil, i.e., it removes any fixed irradiance pattern.

The scintillation index is defined as the variance of the normalized irradiance distribution:

$$\sigma_{\overline{\mathcal{I}}}^2 = \mathrm{Var}(\overline{\mathcal{I}}) = \langle (\overline{\mathcal{I}} - \langle \overline{\mathcal{I}} \rangle)^2 \rangle = \frac{\langle \overline{\mathcal{I}}^2 \rangle}{\langle \overline{\mathcal{I}} \rangle^2} - 1. \tag{5}$$

The variance of the normalized irradiance field can be computed either as a sample variance of the normalized pixel values or from the integral of their power spectral density. For the spatial scintillation index, the sample variance is computed for all pixels in the pupil for each acquisition and then the resulting variances are averaged for all realizations:

$$\sigma_{\overline{\mathcal{I}}}^2 = \langle \mathrm{Var}_{x,y}(\overline{\mathcal{I}}(x, y, k)) \rangle_k = \langle \langle (\overline{\mathcal{I}} - \langle \overline{\mathcal{I}} \rangle_{x,y})^2 \rangle_{x,y} \rangle_k. \tag{6}$$

The temporal computation is the same but computed per pixel using all the samples in the time series of every pixel and then averaged across all pixels:

$$\sigma^2_{\bar{\mathcal{I}}} = \langle \mathrm{Var}_k(\bar{\mathcal{I}}(x,y,k)) \rangle_{x,y} = \langle \langle (\bar{\mathcal{I}} - \langle \bar{\mathcal{I}} \rangle_k)^2 \rangle_k \rangle_{x,y}. \tag{7}$$

We also compute the spatial and temporal power spectral density (PSD) of the scintillation patterns. For the spatial characterization, we compute a 2D PSD (using a 2D fast Fourier transform) for every acquisition and then we compute the average of the 2D PSDs of all acquisitions. After computation of the azimuthal average, the spatial PSD is reported as a one-dimensional (1D) PSD. For the temporal PSD computation, we compute the 1D PSD (using the Welch method) of the per-pixel irradiance time series and then take an average of all PSDs for all pixels.

For the temporal characterization, we also provide the pupil-averaged flux. To compute this, we do a spatial average of the normalized irradiance across all pixels for every acquisition, obtaining a unique time series that is analyzed as the per-pixel time series. This is a proxy measurement of the effect of scintillation on the flux measurement of a mono-detector on the focal image plane but computed on the pupil plane from the measurement of the matrix detector. This measurement may be of interest to assess the performance of mono-detectors in these conditions. Nevertheless, this approximation neglects the variation of the angle of arrival, which may lead to a loss of flux if the mono-detector is not large enough.

4.2.4 *Spatial scintillation results*

The left column of Fig. 5 presents the spatial 1D PSD for PS2, PS3, and the three-screen profile, respectively. The solid line labeled PICOLO, corresponds to the experimental measurements, and the dashed line, labeled TURANDOT, depicts the numerical simulation result. In all cases, both lines overlap for the most part. At least three different factors can explain these deviations: (1) The manufacturing defects and limitations of the phase screens, (2) the presence of noise in the irradiance measurements, and (3) the presence of aliasing due to the finite sampling of the irradiance. In any case, those deviations do not result in strong deviations of the total variance; Fig. 6 shows this by reporting the cumulative integral for each of the PSD. Note also that the low and high frequencies have low power and their contribution to the variance is small, so is the contribution of any small difference between the spectra.

With respect to the manufacturing process effects, the highest spatial frequency present in the phase screens is about 60 cycles/m, corresponding to a 40 μm pixel size in the phase screens with a 2 mm beam diameter and an equivalent 0.4 m telescope diameter on sky. Any frequency beyond that one is not supposed to be correctly represented by the phase screen; in addition, the phase screens were subject to a subpixel smoothing process by the manufacturer to remove high-frequency defects. This process could also affect the spatial frequencies close to the end of the spectrum.

Regarding measurement noise, we can distinguish two different contributions: detector read-out noise and photon noise. Detector read-out noise can be estimated by taking dark frames with the characterization camera and its PSD subtracted from the irradiance one. The presented data were corrected from the data, although its effect is negligible in the variance and in the power spectral densities. The contribution of photon noise cannot be easily estimated since by definition the irradiance measurements under strong scintillation have a high dynamic range; it is therefore not possible to measure the spectrum of this contribution, and the measurements reported contain this signature.

The presence of aliasing has not been quantified either. In conclusion, although it is not possible to allocate the deviations measured to one of the possible causes stated, those are small and have a negligible contribution to the scintillation index. Instead, we highlight the good fitting of all the cut-off frequencies that define the main spectrum features. Since PS2 is stronger in turbulence, it is closer to scintillation saturation and, therefore, the PSD of the spatial scintillation presents two regimes with cut-offs[46,47] at a spatial frequency proportional to $r_0/\lambda z$ and $1/r_0$, whereas the weaker PS3 has its only cut-off at a spatial frequency proportional to $1/\sqrt{\lambda z}$, where z is the propagation distance from the layer to the telescope pupil plane.

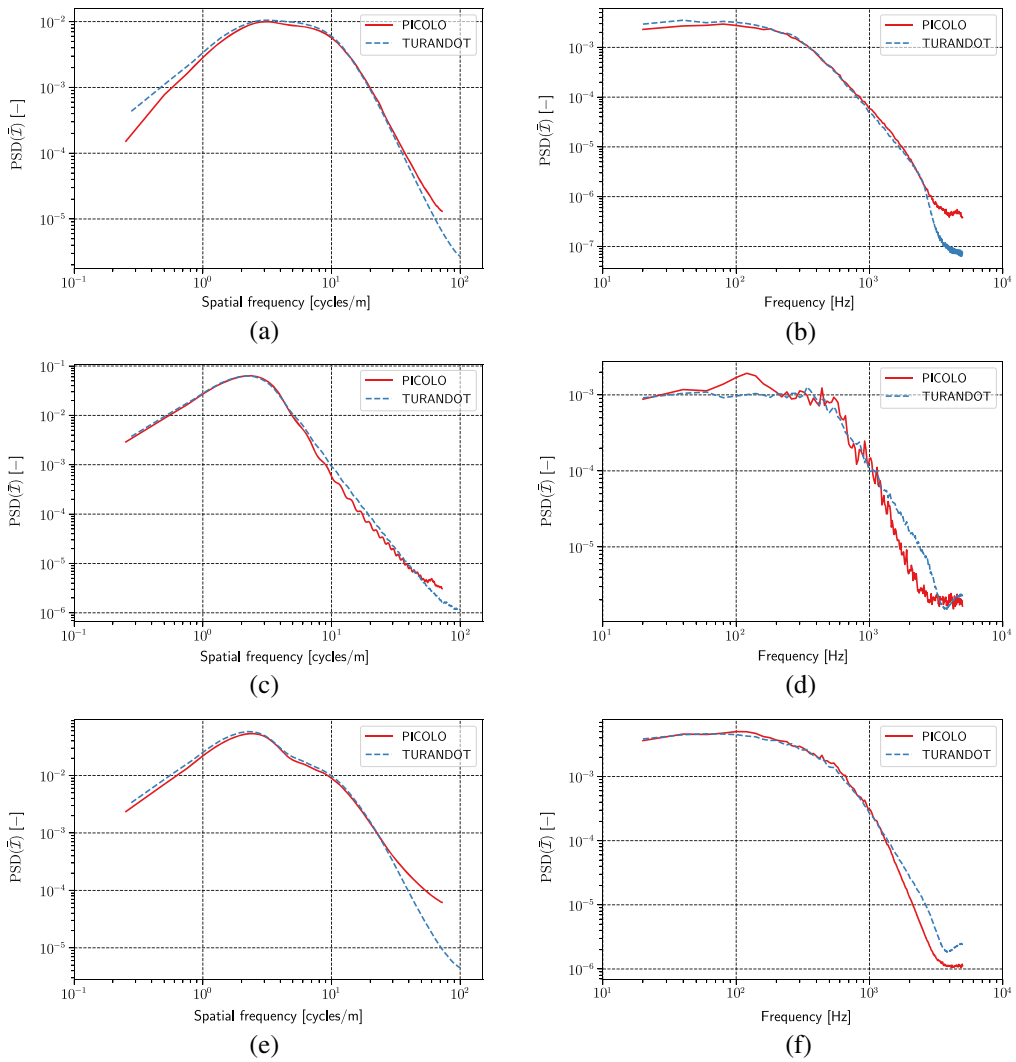

Fig. 5 Spatial and temporal 1D power spectral densities of the normalized irradiance distributions produced by the phase screens. (a) Spatial, PS2 at P2, (b) temporal, PS2 at P2, (c) spatial, PS3 at P3, (d) temporal, PS3 at P3, (e) spatial, three-screen configuration, and (f) temporal, three-screen configuration.

Table 5 provides a comparison of the spatial scintillation indices for both numerical simulation and experiment. The scintillation index is computed as the sample variance of the normalized irradiance measurements (see Sec. 4.2.3). For PS1, the expected scintillation index is zero since the screen is located at the pupil of the telescope and there is no propagation distance. This is the case in the numerical simulation, whereas in the experimental setup, we measure some scintillation. The reason for this is twofold. First, it is not physically possible to place the screen exactly at the pupil, so there is some propagation. For example, the same screen placed at a distance of 1 mm from the telescope pupil results in an equivalent distance of 40 m on sky and would lead to a scintillation index of 0.064. Second, some diffractive effects are observed (see filament-like structures in the pupil PS1 image in Fig. 3) that also contribute to the inhomogeneity of the pupil illumination. Nevertheless, as can be observed in the three-screen configuration, the scintillation from phase screen 1 does not result in a significant contribution.

Regarding the uncertainty quantification of the results, we provide the error bars for the numerical simulation. The uncertainty of the numerical simulation is due to the statistical convergence of the results. For the computation of the error bars, we used a bootstrapping method, where we divided the available number of samples in groups and computed the average scintillation index from it, where the error bars correspond to the standard deviation among all results.

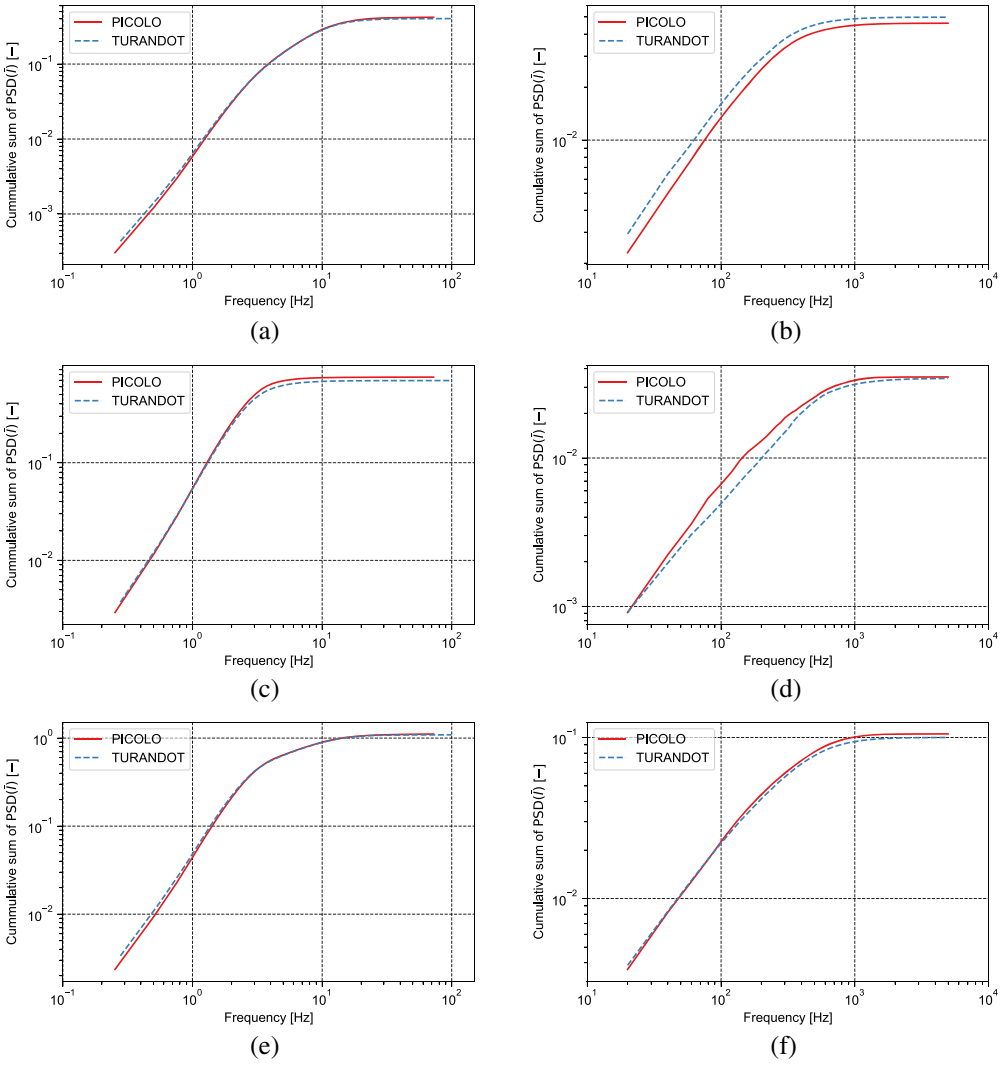

Fig. 6 Cumulative sum of spatial and temporal 1D power spectral densities of the normalized irradiance distributions produced by the phase screens. (a) Spatial, PS2 at P2, (b) temporal, PS2 at P2, (c) spatial, PS3 at P3, (d) temporal, PS3 at P3, (e) spatial, three-screen configuration, and (f) temporal, three-screen configuration.

Table 5 Spatial scintillation index comparison between numerical simulation and experiment.

	PS1	PS2	PS3	All
TURANDOT	0.000 ± 0.000	0.985 ± 0.006	0.767 ± 0.018	2.050 ± 0.020
PICOLO	0.102	0.972	0.770	2.090

4.2.5 *Temporal scintillation results*

The right column of Fig. 5 presents the temporal 1D PSD for PS2, PS3, and the three-screen profile. The solid line labeled PICOLO, corresponds to the experimental measurement, whereas the dashed line, labeled TURANDOT, depicts the numerical simulation result. In all cases, the cut-off frequency[45] is proportional to $V/\sqrt{z/k}$, with V the transversal velocity of the layer, and $k = 2\pi/\lambda$ the angular wavenumber. The experimental curves show in this case a noise floor at high frequencies, especially for PS2, where the curve has a different floor to the noise floor from the simulation. The causes for these noise floors are the same as for the spatial spectra since the temporal spectra are given by filtering of the spatial spectra due to the shifting of the layers.

Table 6 Temporal scintillation index comparison between numerical simulation and experiment.

	PS1	PS2	PS3	All
TURANDOT	0.000	1.056	0.692	2.055 ± 0.052
PICOLO	0.101	0.968	0.765	2.138

Both PS3 and the three-layer case show in the TURANDOT case a bump on the high frequencies due to a simulation artifact currently being analyzed. Apart from this, the fit of the curves and their cut-offs shows a satisfactory agreement between the simulation and experiment.

Table 6 provides a comparison of the temporal scintillation indices for both numerical simulation and experiment. The scintillation index is computed as the sample variance of the normalized irradiance measurements (see Sec. 4.2.3). Note that, following the ergodicity hypothesis, the scintillation indices in this table should be the same as the spatial scintillation indices reported in Table 5, which proves to be consistent with our results. We provide the error bars for the temporal simulation with all phase screens computed as the standard deviation of the scintillation indices computed for five simulations of the same case with different random seeds for the phase screen generation.

Finally, we study the variation of the integrated flux after PICOLO. This computation is based on the time series resulting from the averaging of the intensity measurements for every pupil pixel at every frame. Note, this is not an equivalent of the coupled flux since it does not take into account the phase and amplitude effects in the coupling into a single mode fiber. Even with perfect AO (i.e., phase) correction, the mismatch between the wavefront amplitude and the Gaussian mode of the fiber will cause further losses that are not accounted for in this measurement. This measurement is closer to the flux measured by a mono-detector big enough that the variation of the angle of arrival due to turbulence and the PSF size does not cause a loss of flux during the measurement of the time series, i.e., the power in the bucket at the telescope aperture level.

Figure 7 shows a part of the time series obtained, both for the experiment, labeled PICOLO, and the numerical simulation, labeled TURANDOT. The time series is further analyzed by computing its PSD, shown in Fig. 8, whereas a histogram of the time series is shown in Fig. 9. The comparison of the PSD shows how the time series have the same time characteristics, including the two regimes with cut-offs around 500 and 1000 Hz. At high frequencies, the experimental results a similar noise floor to the one observed in the temporal spectra. The same high-frequency noise presence can be observed in the time series plot. The shape of the histograms is similar too and the variance of the power (reported in the same figure), equivalent to the scintillation index of the irradiation pattern filtered by the pupil, is also close.

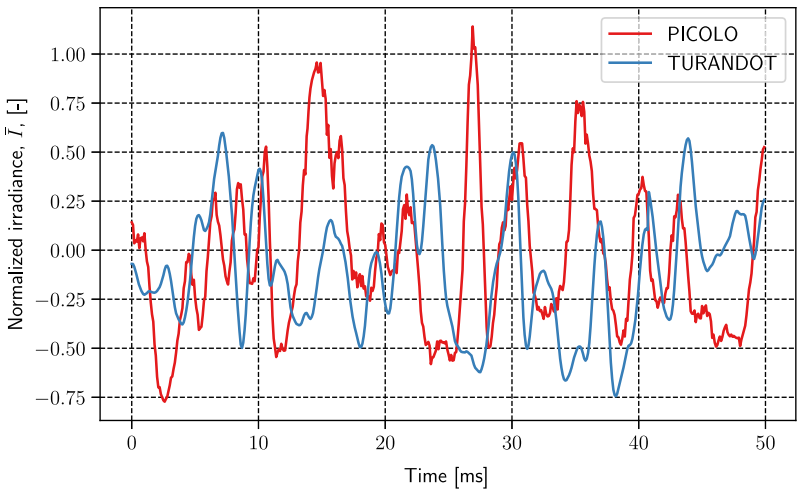

Fig. 7 Zoom in on the time series of the pupil averaged flux.

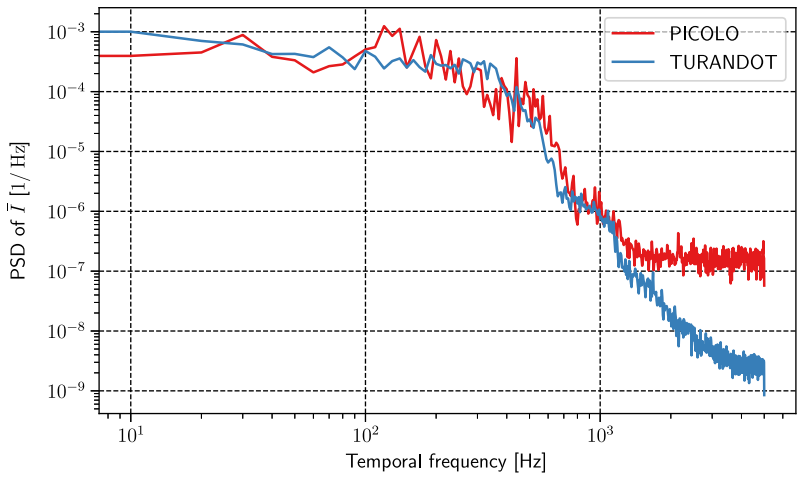

Fig. 8 Power spectral density of the time series of the pupil averaged flux.

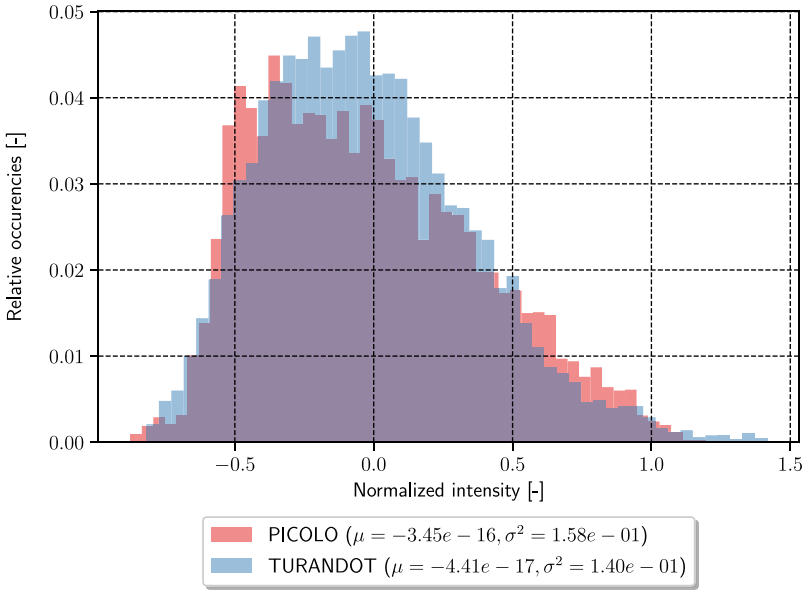

Fig. 9 Histogram of the time series of the pupil averaged flux.

We take this opportunity to discuss the periodicity of the turbulence generated. Note that the emulator only uses a small area of the phase screen, which is the ring resulting from the illumination of the circular beam footprint when the screen rotates. The screens rotate to generate the displacement equivalent to the one produced by the wind for each layer. After a given period of time, the screen completes a turn and the beam starts sampling the same phase distortion as previously, generating a periodic behavior. This effect is diminished by the fact that there are three phase screens rotating at different speeds, so the combination of the three reduces the periodicity of the overall turbulence. The previous statement is true for the phase disturbance since the three screens participate in it. We computed the period for this case, and it corresponds to hours, longer than the typical minute scale time series expected from the emulator. Still, for the scintillation, this period is reduced, since only PS2 and PS3 are involved. Note that both phase and scintillation contribute to fiber coupling, so the periodicity of the coupled flux will be impacted. Finally, the case of the pupil averaged flux presented above is the one most affected by periodicity. Since the speckles produced by PS2 are much smaller than the pupil size, their effect is averaged out in this metric, and only the PS3 speckles (similar in size to the pupil) contribute to it. As a result, the pupil-averaged flux shows a periodicity corresponding to the time that it takes PS3 to complete a rotation. For the time series presented above, over a total duration of 1 s we

Table 7 Operating conditions of the turbulence delivered by the emulator.

Name	Value	Comment
Pupil diameter	40 cm	Equivalent telescope size
Wavelength	1.55 μm	—
Exit pupil diameter	3.3 mm	Telescope pupil conjugated to periscope mirror. Interface to client systems
Orbit height	500 km	—
Culmination point	90°	—
Distance to satellite	1965 km	—
Satellite tracking slew rate	2 mrad $\cdot$ s^{-1}	—
Line-of-sight elevation	10 deg	—
r_0	3.39 cm	Sum from the per-layer results in Table 4
D/r_0	11.8	From the r_0 reported above
θ_0	1.603 μrad	Computed from formula for the "measured" profile in Table 3
τ_0	3.125 μs	Computed from formula for the "measured" profile in Table 3
σ_I^2	2.138	Temporal scintillation index, as measured in the characterization (see Table 6)

detected a total of seven periods by computing its autocorrelation, corresponding to the seven rotations of the screen during that amount of time. These periodical effects result from the limitation in the number of phase screens that are used. Once understood and accounted for in the interpretation of the emulator results, such a limitation is deemed acceptable, since to be overcome a greater number of phase screens would be necessary, which would increase the complexity and cost of the setup.

5 Operating Conditions

Table 7 summarizes the effective parameters of the bench after the characterization reported in this work.

6 Conclusion

We have presented the methodology for the design and characterization of a turbulence emulator representative of a downlink between an LEO satellite and a ground station at 10 deg elevation. The bench is able to simulate both the strong turbulence conditions at low elevation, as well as the dynamics due to the fast apparent wind caused by the satellite motion. The emulator is able to host different instruments by coupling them to its exit pupil. Therefore, the emulator is able to provide long time series of the disturbed field at the pupil of a telescope under realistic turbulence conditions.

The characterization presented allowed proving that the bench delivers the turbulence conditions expected. This includes a detailed characterization of the scintillation conditions, which is necessary for future investigations regarding the performance of AO systems under scintillation. The agreement found with respect to the numerical simulation motivates the use of the numerical simulation as a digital twin of the bench for performance estimations before testing components on the bench.

As a result, ONERA has a testing platform for future AO systems (wavefront measurement and control laws) under strong turbulence perturbations (scintillation and unsteady turbulence). ONERA uses this platform for its own research and also offers access to it to the community.[48] The system will be used to test new AO and free-space optical communication concepts and integrate and validate them before on-sky campaigns. For example, the integration and testing

of the AO system for ONERA's FEELINGS ground station[10] study Shack–Hartmann wavefront sensors under scintillation conditions and how to improve their performance, test new AO control algorithms (such as predictive control[49]), test new turbulence correction concepts, such as photonic integrated circuits[48] and test new telecommunication components or digital signal processing architectures. An upgrade of the bench to add the effect of anisoplanatism in the feeder links[50] cases is currently under study.

Disclosures

The authors of this manuscript declare that they have no relevant financial interests in the manuscript of this article and do not have any other potential conflicts of interest to disclose.

Code and Data Availability

ONERA proposes the use of this bench to collaborators for testing their own methods and components.

Acknowledgments

The authors would like to thank Bouchra Benammar (with CNES) for her support and discussions during the elaboration of this work. Pablo Robles' PhD is co-funded by ONERA (the French Aerospace Lab) and CNES (the French Space Agency). This work has been partly funded by ONERA in the frame of the SUSA and TOSSCA internal research projects. This work benefited from the support of the French National Research Agency (ANR) with WOLF (ANR-18-CE31-0018), APPLY (ANR-19-CE31-0011), and LabEx FOCUS (ANR-11-LABX-0013); the Programme Investissement Avenir F-CELT (ANR-21-ESRE-0008), the Action Spécifique Haute Résolution Angulaire (ASHRA) of CNRS/INSU co-funded by CNES, the ECOS-CONYCIT France-Chile cooperation (C20E02), the ORP H2020 Framework Programme of the European Commission's (Grant No. 101004719), and STIC AmSud (21-STIC-09).

References

1. C. Voland et al., "Towards optical data highways through the atmosphere," *Proc. SPIE* **10910**, 109101C (2019).
2. H. Hauschildt et al., "HydRON: high throughput optical network," *Proc. SPIE* **10910**, 109100K (2019).
3. S. Shaklan and F. Roddier, "Coupling starlight into single-mode fiber optics," *Appl. Opt.* **27**, 2334–2338 (1988).
4. D. Giggenbach, "Fading-loss assessment in atmospheric free-space optical communication links with on-off keying," *Opt. Eng.* **47**, 046001 (2008).
5. R. Fante, "Electromagnetic beam propagation in turbulent media," *Proc. IEEE* **63**(12), 1669–1692 (1975).
6. H. T. Yura and W. G. McKinley, "Optical scintillation statistics for IR ground-to-space laser communication systems," *Appl. Opt.* **22**, 3353 (1983).
7. J. D. Barchers, D. L. Fried, and D. J. Link, "Evaluation of the performance of Hartmann sensors in strong scintillation," *Appl. Opt.* **41**, 1012 (2002).
8. M.-T. Velluet et al., "PICOLO: turbulence simulator for adaptive optics systems assessment in the context of ground-satellite optical links," *Proc. SPIE* **11532**, 1153207 (2020).
9. N. Vedrenne et al., "Turbulence effects on bi-directional ground-to-satellite laser communication systems," in *Proc. Int. Conf. Space Opt. Syst. and Appl. (ICSOS)*, p. 6 (2012).
10. P. Cyril et al., "FEELINGS: the ONERA's optical ground station for Geo Feeder links demonstration," in *IEEE Int. Conf. Space Opt. Syst. and Appl. (ICSOS)*, IEEE, Kyoto City, pp. 255–260 (2022).
11. D. M. Boroson and B. S. Robinson, "The Lunar laser communication demonstration: NASA's first step toward very high data rate support of science and exploration missions," *Space Sci. Rev.* **185**, 115–128 (2014).
12. E. Fischer et al., "Development, integration and test of a transportable adaptive optical ground station," in *Proc. Int. Conf. Space Opt. Syst. and Appl. (ICSOS)*, p. 6 (2015).
13. C. Petit et al., "Investigation on adaptive optics performance from propagation channel characterization with the small optical transponder," *Opt. Eng.* **55**, 111611 (2016).
14. A. Brady et al., "Experimental validation of phase-only pre-compensation over 494 m free-space propagation," *Opt. Lett.* **42**, 2679 (2017).
15. B. I. Bitachon et al., "Tbit/s single channel 53 km free-space optical transmission: assessing the feasibility of optical geo-satellite feeder links," in *Eur. Conf. Opt. Commun. (ECOC)*, Optica Publishing Group, p. Th3A.6 (2022).

16. A. M. Bonnefois et al., "Feasibility demonstration of AO pre-compensation for GEO feeder links in a relevant environment," *Opt. Express* **30**, 47179–47198 (2022).
17. Z. Qu and I. B. Djordjevic, "Approaching terabit optical transmission over strong atmospheric turbulence channels," in *18th Int. Conf. Transp. Opt. Networks (ICTON)*, pp. 1–5 (2016).
18. A. Brady et al., "Demonstration of adaptive optical pre-compensation in horizontal tests," in *IEEE Int. Conf. Space Opt. Syst. and Appl. (ICSOS)*, pp. 1–5 (2019).
19. K. Kudielka, E. Fischer, and T. Dreischer, "Numerical prediction and experimental validation of irradiance fluctuations in a pre-compensated optical feeder link," *Proc. SPIE* **11180**, 111805N (2019).
20. G. DiComo et al., "Implementation of a long range, distributed-volume, continuously variable turbulence generator," *Appl. Opt.* **55**, 5192–5197 (2016).
21. L. Jolissaint, "Optical turbulence generators for testing astronomical adaptive optics systems: a review and designer guide," *Publ. Astron. Soc. Pac.* **118**, 1205 (2006).
22. D. J. Butler et al., "Phase screens for astronomical multiconjugate adaptive optics: application to MAPS," *Proc. SPIE* **4839**, 623–634 (2003).
23. S. V. Mantravadi, T. A. Rhoadarmer, and R. S. Glas, "Simple laboratory system for generating well-controlled atmospheric-like turbulence," *Proc. SPIE* **5553**, 290–300 (2004).
24. S. Thomas, "A simple turbulence simulator for adaptive optics," *Proc. SPIE* **5490**, 766–773 (2004).
25. S. Hippler et al., "The MPIA multipurpose laboratory atmospheric turbulence simulator MAPS," *Proc. SPIE* **6272**, 627255 (2006).
26. L. Roberts et al., "First results from the adaptive optics system for LCRD's optical ground station one," in *Adv. Maui Optical and Space Surveillance Technologies Conf. (AMOS)*, Maui, Hawaii, S. Ryan, Ed., (2018).
27. E. Mieda et al., "Multiconjugate adaptive optics simulator for the thirty meter telescope: design, implementation, and results," *J. Astron. Telesc. Instrum. Syst.* **4**, 049002 (2018).
28. L. Zhou et al., "Mitigating effect on turbulent scintillation using non-coherent multi-beam overlapped illumination," *Opt. Laser Technol.* **97**, 97–105 (2017).
29. R. Rampy et al., "New method of fabricating phase screens for simulated atmospheric turbulence," *Proc. SPIE* **7736**, 77362Y (2010).
30. S. Hippler et al., "Atmosphere-like turbulence generation with surface-etched phase-screens," *Opt. Express* **14**, 10139–10148 (2006).
31. C. Rickenstorff, J. A. Rodrigo, and T. Alieva, "Programmable simulator for beam propagation in turbulent atmosphere," *Opt. Express* **24**, 10000–10012 (2016).
32. M. K. Giles et al., "Setting up a liquid crystal phase screen to simulate atmospheric turbulence," *Proc. SPIE* **4124**, 89–97 (2000).
33. C. M. S. Corley, M. Nagashima, and B. N. Agrawal, "Beam control and a new laboratory testbed for adaptive optics in a maritime environment," in *IEEE Aerosp. Conf.*, pp. 1–13 (2010).
34. R. K. Tyson and B. W. Frazier, "Microelectromechanical system programmable aberration generator for adaptive optics," *Appl. Opt.* **40**, 2063–2067 (2001).
35. O. Keskin, L. Jolissaint, and C. Bradley, "Hot-air optical turbulence generator for the testing of adaptive optics systems: principles and characterization," *Appl. Opt.* **45**, 4888–4897 (2006).
36. D. J. Geisler et al., "Atmospheric emulation and testing methodology for laboratory verification of FSO communications transceivers," in *IEEE Int. Conf. Space Opt. Syst. and Appl. (ICSOS)*, pp. 1–5 (2019).
37. L. Canuet et al., "Statistical properties of single-mode fiber coupling of satellite-to-ground laser links partially corrected by adaptive optics," *J. Opt. Soc. Am. A* **35**, 148 (2018).
38. P. Lognoné et al., "Phase estimation at point-ahead angle for AO pre-compensated ground to GEO satellite telecoms," *Opt. Express* **31**, 3441–3458 (2022).
39. G. C. Valley, "Isoplanatic degradation of tilt correction and short-term imaging systems," *Appl. Opt.* **19**, 574 (1980).
40. O. J. D. Farley et al., "Identifying optical turbulence profiles for realistic tomographic error in adaptive optics," *Mon. Not. R. Astron. Soc.* **488**, 213–221 (2019).
41. J. Chabé et al., "PML: a generalized monitor of atmospheric turbulence profile with high vertical resolution," *Appl. Opt.* **59**, 7574–7584 (2020).
42. D. Saxenhuber et al., "Comparison of methods for the reduction of reconstructed layers in atmospheric tomography," *Appl. Opt.* **56**, 2621–2629 (2017).
43. A. Tokovinin, "From differential image motion to seeing," *Publ. Astron. Soc. Pac.* **114**, 1156 (2002).
44. R. Cubalchini, "Modal wave-front estimation from phase derivative measurements," *J. Opt. Soc. Am.* **69**, 972 (1979).
45. L. C. Andrews and R. L. Phillips, *Laser Beam Propagation through Random Media*, 2nd ed., SPIE Press, Bellingham, Washington (2005).
46. L. C. Andrews et al., "Theory of optical scintillation," *J. Opt. Soc. Am. A* **16**, 1417 (1999).
47. M. Sechaud et al., "High-resolution imaging through atmospheric turbulence: link between anisoplanatism and intensity fluctuations," *Proc. SPIE* **3866**, 100–109 (1999).

48. A. Billaud et al., "Turbulence mitigation via multi-plane light conversion and coherent optical combination on a 200 m and a 10 km link," in *IEEE Int. Conf. Space Opt. Syst. and Appl. (ICSOS)*, IEEE, Kyoto City, pp. 85–92 (2022).
49. P. Robles et al., "Predictive adaptive optics for satellite tracking applications: optical communications and satellite observation," *Proc. SPIE* **12185**, 121852S (2022).
50. N. Vedrenne et al., "Adaptive optics pre-compensation for GEO feeder links: towards an experimental demonstration," in *IEEE Int. Conf. Space Opt. Syst. and Appl. (ICSOS)*, IEEE, Naha, pp. 77–81 (2017).

Pablo Robles received his BSc degree from the University of León, Spain, and his MSc degree in Technical University of Munich, Germany, in aerospace engineering. He is a PhD student in optical instrumentation at ONERA, France, working on adaptive optics for LEO-to-ground laser communications. His research interests are adaptive optics, imaging science, and spaceborne optical instrumentation.

Biographies of the other authors are not available.